The influence of graphene oxide on the microstructure and properties of ultrafine-grained copper processed by high-pressure torsion

Maria Emerla[1], Piotr Bazarnik[1]*, Yi Huang[2,3], Anita Wojciechowska[1], Marta Ciemiorek[1], Jarosław Pura[1], Monika Wieczorek-Czarnocka[1], Purbayanto Muhammad Abiyyu Kenichi[1], Agnieszka Jastrzębska[1], Małgorzata Lewandowska[1], Terence G. Langdon[2]

1 Warsaw University of Technology, Faculty of Materials Science and Engineering, Wołoska 141, 02-507 Warsaw, Poland

2 Materials Research Group, Department of Mechanical Engineering, University of Southampton, Southampton SO17 1BJ, United Kingdom,

3 Department of Design and Engineering, Faculty of Science and Technology, Bournemouth University, Poole, Dorset BH12 5BB, United Kingdom

* piotr.bazarnik@pw.edu.pl

Abstract

New metal matrix nanocomposites with enhanced thermal stability were produced in a three step process consisting of mechanical milling, spark plasma sintering and High-Pressure Torsion (HPT). The nanocomposites consisted of a copper matrix and the addition of 1 wt.% Graphene Oxide (GO) as a reinforcement. A nanocrystalline microstructure, enhanced hardness and improved thermal stability were achieved. The grain size of the nanocomposites was ~55 nm which is almost four time smaller than for Cu HPT at 210 nm. Hardnes and ultimate tensile strength of the nanocomposites reach 250 Hv and 700 MPa, respectively, which was more than three times higher than for the initial material. The most important result is that the nanocomposites remained ultrafine-grained up to 500 ºC whereas the Cu HPT fully recrystalized after annealing at 300 ºC The report also includes an investigation of the electrical conductivity of the copper-based composite which was slightly better than for copper after HPT together with the wear behaviour of this material. This is one of the first reports on copper reinforced with graphene oxide composites produced by HPT and it gives information on its thermal stability, electrical conductivity and wear behaviour together with the microstructural characteristics and mechanical properties.

Keywords: Copper, Graphen Oxide, High-Pressure Torsion, metal matrix composites, thermal stability

1. Introduction

The modern industry places increasing demands on structural materials so that new approaches to materials development are a pressing requirement. Novel fabrication techniques allow combined properties and provide a potential for new functionalities. One of the directions in this field is to increase the strength of the metals through grain size reduction[1–4]. It is well known that intense grain refinement to the ultrafine-grained (UFG) or nanocrystalline (NC) level leads to a significant increase in strength, as described by the Hall–Petch relationship [5,6]. In practice, UFG and NC materials are most readily produced in bulk form by subjecting materials to severe plastic deformation (SPD). A number of techniques are now available for the SPD processing of metals [2–4,7–11] The most promising in terms of producing novel metallic structures with the smallest possible grain sizes is high-pressure torsion (HPT) [2,4]. HPT is considered the most effective for achieving UFG and NC structures because of the processing ability to generate extremely high strains [12,13].

Despite a very significant increase in strength, UFG and NC materials generally exhibit some disadvantages. For example, it was proven that in SPD processing the grain size decreases with increasing strain until it reaches a stable minimum which is designated the saturation state. This limitation in grain refinement has attracted much attention [14–19] and it appears to be an inherent feature of each material depending upon the crystallographic structure, stacking-fault energy, purity level of the alloy or the presence of intermetallic impurities. Moreover, the commercial applications of the UFG/NC alloys are limited due to their low microstructural stability at elevated temperatures which complicates the processing of final products in industry. Due to the high energy stored in these materials in the form of defects such as grain boundaries or dislocations, they are inherently thermally unstable and annealing, even at low temperatures, leads to recrystallization and coarsening of the microstructure, which in turn degrades the material properties [20–22]. In extreme cases, as in ultra-pure copper after HPT processing, the material recrystallizes already at room temperature [15].

Overcoming the problem of insufficient thermal stability and grain refinement limitations in UFG and NC materials is currently a challenge in materials science. Different physical phenomena could allow the control of grain growth and the stabilization of the structure. One of the most effective approaches is to use nano-

particles uniformly distributed within the metal matrix that will have a pinning effect on any lattice defects, such as dislocations and grain boundaries, thereby stabilizing the UFG microstructure and expanding the temperature window for their potential technological applications [23–25]. Moreover, it has been proven that the addition of dispersed nanoparticles can overcome the saturation effect, leading to a further grain size reduction during SPD processing [26]. However, most studies omit the thermal stability of metal matrix composites (MMCs) while focusing on the synthesis and impact of reinforcement on the microstructural development. By contrast, only a few reports focus on systematic studies to improve the thermal stability in UFG/NC metals reinforced with dispersed particles [23,24,27].

There are several reports regarding HPT processing of composites reinforced with various oxide and carbide particles [23,24,28–32] and composites reinforced with carbon-based particles such as fullerenes [33] or carbon nanotubes [27,34]. Recently, a new group of composites was introduced reinforced with graphene nanoparticles (GNPs) [35–37] or graphene-oxide (GO) nanoparticles [38]. Research on Al-GNPs [37] and Cu-GNPs [39] fabricated by HPT processing shows the general trend that the addition of even small amounts (1-2%) of graphene produces a remarkable increase in the mechanical properties, a decrease in the coefficient of friction, an improvement in the electrical conductivity [39] and even an improvement in the wear resistance [39], when compared with pure metals after HPT processing [40,41]. In practice, GO is easier to produce and easier to uniformly distribute in a Cu matrix than graphene due to oxide functional groups on the GO surface. Moreover, it has been reported that the oxygen groups in GO have a tendency to create a strong bonding with the metallic matrix whereas in graphene-based composites this connection is weakened [39,42–44]. At the same time, there are only a few publications covering copper-based composites reinforced with GO and none of them focuses on composites produced by HPT. Accordingly, the present study was therefore initiated to evaluate the use of HPT processing in the fabrication of Cu-GO composites as well as evaluating their mechanical properties, electrical conductivity and thermal stability.

2

2. Materials and Methods

2.1. Materials

The Cu-GO nanocomposites were produced in a three-step process consisting of: 1) a mixing of the powders by mechanical milling, and then 2) sintering by a Spark Plasma Sintering (SPS) method and finally 3) processing by HPT.

A regular-shaped copper powder (produced by ABCR company) with a purity of 99% and a particle size of ~50 ± 13 μm was used as the matrix. The composites were reinforced by adding 1 wt.% of GO flakes produced by modification of Hummers method which was described in another report [45]. The powders were mixed in a planetary ball milling system (Retsch PM100) in an argon protective atmosphere with a speed of 300 rpm and time of 1 h. The weight ratio of powder to ball was 1:10. The milling chamber and balls were made of ZrO_2.

2.2. Fabrication

The powders were consolidated by the SPS technique using a graphite die with a sample diameter of 10 mm and a height of 10 mm. The sintering process was carried out at a temperature of 950 °C in an argon atmosphere with a heating rate of 100 °C/min and a 15 min holding time at maximum temperature and a pressure of 50 MPa. As a reference, a sample of pure copper (denoted as Cu SPS) was sintered under the same conditions. Fig.1 illustrates the microstructure of this sample where it consists of large grains of about 27 ± 10 μm with twins and many round-shaped pores with average diameters of about 1μm. The density of this sample measured by the Archimedes' method was 8.44 g/cm^3 which is about 95% of the theoretical density of copper.

The sintered samples were cut with a circular saw into discs of 10 mm diameter and 1 mm height and then subjected to HPT processing. This processing was conducted under an applied pressure of 6.0 GPa at room temperature under quasi-constrained conditions [46]. Discs were torsionally strained by rotating the lower anvil at 1 rpm through 20 revolutions for the Cu-GO nanocomposite and for the Cu reference sample. Potential slippage and temperature rise during HPT were controlled according to standards from previous studies [47–49].

2.3. Characterization

The microstructures of Cu and the Cu-GO composites were examined using scanning electron microscopy (SEM) (Hitachi Su8000) operating at an accelerating voltage of 10 kV in back-scattered electron (BSE) mode and secondary electron (SE) mode. The SEM observations were carried out on cross-sectional planes of the discs in an area ~1 mm from the disc edge. The samples for SEM observations were prepared by ion milling polishing on Hitachi IM4000. This procedure gives a high quality surface without any deformation, stresses and/or the formation of oxide layers, and it allows the structure to be observed in so-called channel contrast in the SEM. Detailed structural investigations were complemented using scanning electron transmission microscopy (STEM) Thermo-Fisher Scientific SPECTRA 200, with a dedicated Cs-corrected high resolution microscope operating under an accelerating voltage of 200 kV and equipped with Super-X energy dispersion spectroscopy (EDS) detectors. The samples for STEM observations were cut using a focus ion beam (FIB) microscope Hitachi NB-5000. Structural investigations were complemented with Raman spectroscopy in order to confirm the presence of GO particles in the composites. Firstly, the GO flakes were tested, then the mixed powders and finally the composites after HPT. The tests were conduct on a spectroscope produced by Renishaw company with a laser wavelength of 514 nm.

The mechanical properties of HPT-processed samples were evaluated using microhardness measurements, tensile testing and wear testing. The Vickers microhardness, Hv, was measured along radial directions on the polished disc surfaces using a Falcon 503 microhardness tester. The measurements were taken under a load of 200 g and dwelling time 10 s along randomly selected diameters on each disc with a spacing of 0.3 mm between the measuring points. The results were plotted in the form of the hardness profiles. The tensile tests were carried out on microsamples cut from discs by electrical discharge using a universal testing machine Zwick Z005 with an initial strain rate of 10^{-3} s^{-1}. For each state at least two samples were cut and tested. The gauge sections of the samples were 4 mm long and the cross-sections were 0.6×0.8 mm^2. A Digital Image Correlation system was used for the tests in order to accurately measure the elongations.

The wear behaviour was examined in a reciprocating sliding condition by pin-on-plate testing with the use of NC6 steel as the contra material with a hardness of 270 Hv (PN-EN ISO 4957). The pin diameter was 3 mm and its surface was prepared by grinding on 1000 paper. The test was conducted under a load of 3 kg and time of 8 h at room temperature in an air atmosphere without the use of a lubricant. The range of motion of the pin along the disc was 8 mm, the number of cycles was 28800, the frequency was 1 Hz and the total friction path was 345.6 m. All samples were weighed before and after the wear test. After the test, the abrasion surface was examined using a profilometer (Wyko NT9300 optical profilometer from Veeco) and SEM method. For comparative reasons the friction coefficient and wear rate were calculated. The friction force was measured directly by the wear test device in N and the friction coefficient was then calculated by dividing the friction force in N by using the load in N. The wear rate was calculated by dividing the volume of the wiped sample material by the pressing force multiplied by the friction distance.

Samples for the electrical conductivity test were prepared by grinding and finishing the surface by polishing with a diamond suspension of 1 um. The electroconductivity measurements were conducted by a four-point method using a digital multimeter (Keithley DAQ6510, USA). The measurements were taken at three different spots and the reported electrical conductivity was obtained by taking the average of these values. This method involves the use of four probes in a single line with known equal spacing between them of 2 mm. The flow of current between the two outer probes causes a reduction in the voltage between the two inner probes and, by measuring this change, it is possible to determine the resistance of the sample and thus determine its electrical conductivity. The resistance was measured in Ohm and related to the dimensions of the probes in meters, and the inverse of this value is then the conductivity of the probes expressed in Simens per metre.

The thermal stability was investigated by annealing the samples for 1 hour in a 100-500 ºC temperature range. After annealing, the hardness of the samples was measured in the same manner as for the samples before annealing. Thereafter, the microstructure was investigated by SEM and STEM with the sample preparation and the observations made in the same way as for the unannealed samples.

3. Results

3.1. Microstructure characterization

Fig. 2 a, b shows SEM BSE microstructural images of the pure Cu and Cu-GO nanocomposite both after HPT. The average grain size in pure copper (Fig. 2a) was 210 nm and this is consistent with the results reported for materials processed using conventional SPD methods [40]. The addition of GO led to more intense grain refinement (Fig. 2b) and the resultant grain size was too small to be visible in the SEM images. At the same time, some GO agglomerates were detected in the microstructure (black in BSE contrast in Fig.2b) but their sizes was not larger than ~500 nm and they covered less than 1.5% of the composite surface area.

The SEM structural investigations of the Cu-GO nanocomposite were complemented with STEM studies. Fig. 2 c, d shows exemplary STEM images of the microstructure of the Cu-GO composite in bright-field (BF) and high-angle annular dark field (HAADF) modes, respectively. The BF mode image (Fig.2c) shows a highly refined structure of the Cu matrix consisting of equiaxed grains containing a high concentration of dislocations. The average grain size determined from these images was ~55 nm. On the other hand, the HAADF image (Fig. 2d) demonstrates the distribution of GO nanoparticles (the dark regions in the HAADF image) in the matrix. It is apparent that the large GO flakes were fragmented during milling and HPT processing and this reduced them to smaller flakes that were uniformly distributed in the Cu matrix. The size of these particles varied in the range of 5-30 nm.

In order to prove that the particles visible in the SEM and STEM images are GO, Raman spectroscopy studies were conducted. Based on the literature data [50–54] graphene oxide may exhibit a few characteristic peaks in Raman spectroscopy where the disorder band arises from a tangential stretch and sp^3 – hybridized carbon called D band approximately at 1355 cm^{-1} and a second band called G at 1575 cm^{-1} representing the crystalline graphite [55]. It is also found in the literature that the 2D band can be located at about 2700 cm^{-1} [51] but this is not considered in the present analysis because the most significant changes occur within the G and D peaks. When it comes to analysing the GO Raman spectra, the ratio between the D and G band intensity (ID/IG) is the most important. Thus, for GO the ID/IG is lower than 1 (0.85)

and the increasing value of the ID/IG ratio is connected with the higher defect level resulting in the degradation of GO [50,51,56].

Fig.3 represents the Raman spectra collected for the GO flakes, for a mixture of copper powder and GO after mechanical milling and on the samples after HPT. It is apparent that GO was detected in all three samples but the ratio ID/IG was different. Initially GO was lower than 1 and it increased with further processing steps such as ball milling (1.03) and HPT (1.37). This means that the mechanical milling of GO with Cu powder, SPS and HPT processing led to an increase in the density of defects in the GO structure and therefore to its partial degradation.

3.2. Mechanical properties of Cu-GO nanocomposites

The results of microhardness measurements on the disc cross-sections are presented in Fig. 4 as a function of distance from the disc centre for the Cu-GO nanocomposite together with data for pure Cu after SPS and after HPT processing. The hardness for pure Cu samples after HPT rose more than three times from 55 Hv units to more than 180 Hv units compared with the sample after SPS. It is also apparent that the addition of GO significantly impacts the microhardness leading to its further increase by 70-80 Hv units compared to pure Cu after HPT. The microhardness of the Cu-GO nanocomposite exceeds 260 Hv units.

The results of tensile testing for the HPT-processed composite are illustrated in Fig. 5 where these data are complemented by including results for Cu sample both after SPS and after 20 HPT revolutions. The HPT processing leads to a more than two-fold improvement in the mechanical strength of Cu SPS such that its yield strength increased from 140 MPa for the sample after SPS to 640 MPa after HPT processing. The highest mechanical strength was observed for the Cu-GO nanocomposite sample at almost 700 MPa. However, this sample underwent a brittle fracture with no plastic deformation in tension. Nevertheless, the maximum stress at which the fracture occurred was higher than the ultimate tensile strength of the HPT processed Cu where these values were 675 and 640 MPa, respectively. Another difference in mechanical properties of the analysed materials can be observed for the strain hardening ability. The curve for Cu after SPS is typical for materials with excellent strain hardening ability but HPT processing decreases this ability and a decrease of stress is observed for

strains higher than approximately 0.02. A further decrease in strain hardening ability is observed for the Cu-GO composite which is not capable of any plastic strain.

3.3. Electrical conductivity

Because of the use of Cu-based nanocomposites in electrical contact materials, their electrical conductivity is considered as a critical property. The results of electrical conductivity of the fabricated Cu-GO nanocomposite, together with the conductivity for Cu SPS and Cu HPT, are presented in Fig 6. The tests show that for Cu after SPS there is a significant decrease of conductivity when compared to the literature data for Cu 99% after casting (a drop from 4.2 E7 S/m [57] to 1.1 E7 S/m) but after HPT processing the electrical conductivity rises to 1.5 E7 S/m. The addition of GO to copper contributes to a further improvement in the conductivity when compared with pure Cu after HPT, as shown in Fig. 6.

3.4. Wear properties

The results obtained in wear tests for Cu SPS, Cu–HPT and the Cu-GO HPT nanocomposite are summarised in Table 1. After the tests, the abrasion surfaces were examined using an optical profilometer and SEM method and the results are presented in Fig. 7 and 8, respectively.

The results suggest that the friction coefficient for the Cu SPS and Cu HPT samples are similar but the wear rate was the smallest for the Cu HPT sample. The highest wear rate was observed for the sample after SPS processing but the mass reduction for this sample was the smallest of all analysed materials. This can be explained by the higher porosity of the material after the SPS process. The Cu-GO sample after HPT exhibited a higher friction coefficient, wear rate and mass loss than the Cu sample after HPT processing.

Fig. 7 shows profilometer images of the surfaces after wear tests and this illustrates differences in the wear behaviour of the individual samples. The wipe/scar on the Cu SPS sample had almost a constant depth of about 200 μm along its entire length (Fig. 7a). At the same time, a high outflow of material at the edges of the abrasion was observed in this sample. The bottom of the scar, despite being slightly tilted, was mostly flat, and this contrasts with samples after the HPT process. Wipes on samples after the HPT process (Cu HPT and Cu-GO HPT in Fig.7b and Fig.7c, respectively)

were deeper in the middle sections and shallower at the edge regions of the wipes. This characteristic strengthening of the edges of the HPT discs resulted also in an overall reduction of wear, including a maximum abrasion depth and abrasion volume.

The main difference between the two samples produced by the HPT process was that most wear products from pure Cu remained attached to one end of the scar (Fig.7b), whereas the material from the Cu with 1% GO was entirely separated from the sample (Fig.7c) and the edge was smoother. The bottoms of the scars also showed differences in the wear mechanisms. The entire length of the scar bottom on Cu SPS was covered by deep parallel scratches and a very similar topography appeared on the middle part of the scar on pure Cu after the HPT process. On the sample with 1% GO, however, the bottom of the scar appeared smoother, less scratched, and consisted mostly of small sharp pits/cracks but also it was placed along the direction of the run.

A more in-depth analysis of abrasion marks was performed using a Scanning Electron Microscope. Fig. 8 shows the wear marks visible in the SEM images for coarse-grained copper after SPS, copper after HPT and copper with GO after HPT. The wear marks on the Cu SPS and the Cu produced by HPT processing show typical features of abrasive wear such as furrowing and longitudinal scratching. In some areas the surface appears flattened and larger cavities seem to be closed by a strongly deformed material. The surface of the Cu-GO sample exhibits similar topographical features but with pits or cavities, and in some cases cracks, arranged transverse to the direction of the run to form river-like meandering patterns. These observations suggest that samples with 1% GO exhibit a different wear mechanism which probably involves a different adhesive component.

3.5. Thermal stability

Fig. 9 shows the average hardness measured at the disk edges for the Cu-GO nanocomposites after HPT processing and subsequent annealing at temperatures ranging from 100 °C to 500 °C for 1 h. These results are also complemented with the hardness values for Cu HPT sample. The results show that the Cu HPT sample is thermally stable up to 200 °C which is in agreement with an earlier report [22]. The Cu-GO sample exhibits a different tendency since the hardness values in this sample decrease slightly with increasing temperature. Nevertheless, even after annealing at

500 ºC, the hardness values are at the level of 200 Hv units which is similar to copper after the HPT processing before annealing.

Microstructural observations were carried out in order to explain this phenomenon. A SEM analysis shows that pure copper after HPT recrystalizes at 300 ºC (Fig. 10a), whereas the Cu-GO nanocomposite was structurally stable even at 400 ºC (Fig. 10b) and starts coarsening of grains at 500 ºC (Fig. 10c) but nevertheless it maintains a UFG structure. Moreover, despite grain growth in this sample, it is apparent that there are a number of uniformly distributed darker spots which correspond to the GO flakes in the initial sample. In order to study this effect in more detail, detailed structural investigations were carried out using a STEM microscope. Fig. 11 shows exemplary STEM images of the Cu-GO sample after annealing at 500 ºC. The comparative BF and HAADF (Fig. 11a and b) images confirm the grain growth observed in SEM with an average grain size of ~200 nm and uniformly distributed particles with sizes from 10 to even 50 nm. Closer investigations of these structures (Fig. 11c and d) revealed that they have a core-shell structure. EDS analyses of these regions (Fig.11d), summarised in Table 2, indicates that these structures consist of a carbon-rich core and an oxygen-rich shell zone embedded within the Cu matrix.

4. Discussion
4.1 Fabrication of Cu-GO nanocomposites

A bulk Cu-GO composite with uniformly dispersed GO nanoparticles was obtained by a three-step fabrication processing including the use of quasi-constrained HPT. This processing introduced a remarkable refinement of the GO agglomerates and grains in the Cu matrix. A combination of milling and HPT processing led to a uniform distribution of GO particles having sizes of tens of nanometres while only a small fraction of fine agglomerates remained in the structure. An analysis of the SEM images (Fig. 2) indicated that the surface area fraction of the GO agglomerates with sizes greater than 100 nm was not higher than ~1.5% of the entire surface of the observed samples. The formation of Cu–O–C chemical bonds, whose origin lies is in the reaction between the Cu and the carboxyl or hydroxyl groups on the surface of the GO, may also play a key role in producing a good dispersion of GO nanoparticles in the Cu matrix. It was shown in previous studies that the oxygen atoms on the surface of GO enhance its connection

with Cu which, in the case of Cu pure graphene composites, was reported to be much weaker [39,42–44].

The addition of GO particles also has a beneficial effect on the enhanced grain refinement of the Cu matrix. The fabricated composite has a nanocrystalline structure with a grain size of around 55 nm (Fig. 2c) while for pure Cu after HPT the grain size is about 210 nm (Fig. 2a). The grain size obtained in this study is one of the smallest reported for Cu and Cu nanocomposites fabricated by SPD processing [58]. In case of graphene oxide phase in enhancing the thermal stability of the nanocomposite.

An enhanced grain refinement effect occurring in composite materials during SPD processing is well known and was reported in many earlier studies [2,26,59]. Hard nanoparticles uniformly distributed in the metal matrix produce a pinning effect on the movement of dislocations and grain boundaries, thereby promoting grain refinement and reducing the tendency for dynamic recovery and recrystallization during processing [60,61].

The nanocomposites in this research exhibit unique strength (Fig. 5) and hardness (Fig. 4) when compared with pure coarse-grained and nanostructured copper. This is due to several factors: (1) the enhanced grain size reduction and the relevant Hall-Petch relationship [5,6], (2) the presence of hard, uniformly distributed GO nanoparticles in the matrix [25,27,29] and (3) the increased density of dislocations resulting from the presence of additional obstacles (GO) to their movement [23,62].

4.2 Electrical conductivity and wear properties

This part of the research was designed to investigate the effect of the addition of GO particles on the electrical conductivity of the fabricated nanocomposites. First of all, it was shown that the electrical conductivity of Cu SPS sample is lower than that for Cu 99% after casting [57]. This is connected with two factors: the high porosity after SPS processing as visible in Fig. 1 [63,64] and the potential oxide impurities introduced during sintering or milling. In powder metallurgy, a protective atmosphere generally plays a key role in shaping the properties of the final product. Despite using the best available protective atmospheres, an oxidation of the powder surface may occur which in turn may affect the electrical conductivity.

The electrical conductivity of pure Cu after HPT processing and the Cu-GO composite (Fig.5) was found to be higher by 36% and 54%, respectively, although it remained lower than reported for Cu 99% after casting [57]. The Cu HPT and Cu-GO HPT samples had no visible pores during the SEM observation (Fig. 2) so that the HPT process effectively densifies the material and removes the porosity created during the sintering process. At the same time, these materials may have small amounts of oxides formed during the sintering process. The best electrical conductivity was obtained for the Cu-GO HPT where the addition of 1% GO improved the electrical conductivity.

Regarding the wear properties, Cu after HPT has the highest wear resistance from all of the tested samples (Fig.7, Table 1). From the traditional Archard equation [56], the increase in hardness should improve the wear resistance. The results for Cu SPS and Cu HPT are in accordance with this law but the results for the Cu HPT and Cu-GO HPT samples are contrary. Furthermore, previous studies have shown more contradictory results whereby surface strengthening through microstructure refinement either increased [65–68] or decreased [40,69–71] the wear resistance. For materials processed by HPT, most of the published results show a decrease in wear resistance compared to the coarse-grained materials [40,69–72]. However, in the present research, the coarse-grained material was produced by sintering of powders which produced a high porosity in the material. These pores may be the starting points for slicing of the material during the wear test and this may explain the better wear resistance of the Cu HPT samples.

By contrast, a different wear behaviour was observed in the Cu-GO HPT sample. Literature data suggests any correlation between the material hardness and wear is limited since the hardness is only one of many material parameters that influence the wear [72]. For example, there are several possible reasons for reducing wear resistance in HPT-processed samples including a low ductility and plasticity of the material, a low strain hardening capability, a higher oxidation rate and the presence of non-equilibrium grain boundaries [66]. Results from the present research suggest that the lower ductility (Fig.5) and the lack of a strain hardening capability led to a lower wear rate for the Cu-GO HPT than for the Cu HPT. It is interesting that the GO particles in the fabricated composite failed to improve the wear resistance as was expected from earlier studies [39]. This is probably due to the amount and size of the GO particles which were relatively uniformly distributed in the composite matrix but were too small

to result in a self-lubricity of the material. However, the addition of GO to the Cu matrix changes the wear surface in Fig.8 from an extensive brittle crack delamination in Cu after HPT to a more plastic delamination and river-like surface in the composite.

4.3 Thermal stability of UFG structure

The uniform distribution of GO nanoparticles in the Cu matrix had a major influence not only on the enhanced grain refinement and improvement of mechanical properties of this nanocomposite but also on its thermal stability. The fabricated Cu-GO composite had a stable microstructure up to 500 ºC (Fig.8, Fig.9). At this temperature, limited grain growth occurred but the microstructure remained UFG. By contrast, pure Cu after HPT fully recrystalized after annealing at 200-300 ºC so that the addition of GO extended the stable temperature window by 200 ºC. The remarkable structural stability in the Cu-GO nanocomposite is connected with the uniform distribution of nano-sized GO particles which inhibits grain boundary movement and blocks grain growth [23,61,73,74]. It should be mentioned that similar grain sizes was reported by Horita et al. by subjecting high-purity Cu (99.99% and 99.99999%) to a cryogenic-HPT process [75]. Nevertheless, the thermal stability of these samples after cryogenic-HPT was so poor that they exhibited a self-annealing and significant drop of mechanical properties within a few hours after the HPT processing. This confirms the importance of the presence of the second (in this case GO) phase to ensure the thermal stability of nanometals.

Despite such a significant increase in the thermal stability of the Cu-GO nanocomposite, it is important to note some characteristic microstructural changes occurring in this sample after annealing at 500 °C (Fig.10 and Fig. 11). A characteristic core-shell structure was observed composed of a C-rich core and an O-rich shell embedded in the Cu matrix. The transformation of GO particles into core-shell structures may be connected with the thermal decomposition of GO at high temperatures [56,76–78]. Graphene oxide has functional groups such as hydroxyl, carbonyl epoxy on its surface and edges [79,80]. When exposed to sufficiently high temperatures, these functional groups separate from GO in the form of gases such as CO and CO_2 vapours. This rapid escape of gases leads to a separation of the thicker carbon layers in places where GO was previously located [81,82] and a thermally

enhanced diffusion of O-rich gases into the matrix. This produces a generation of copper oxides (CuO and Cu_2O) as intermediate products surrounding the C-rich core. All these processes lead to an increase in the space previously occupied by GO, where this is evident in the present composites through the appearance of numerous small black dots in the structural images (Fig. 10 and 11).

5. Summary and conclusions

- Cu – GO nanocomposites were successfully produced using HPT processing.
- A relatively good dispersion of GO was obtained within the Cu matrix.
- The GO addition led to an enhanced grain refinement compared to the matrix material. The reduction of grain size and reinforcing effect led to a higher hardness for the composite compared to the matrix material.
- The addition of GO slightly improved the electrical conductivity of copper after HPT processing.
- The fabricated composite was thermally stable up to 400 °C whereas at 500 °C the microstructure of the composite changed, but remained UFG.
- Annealing of the composite at 500 °C led to a slight reduction of hardness by about 50 Hv.

CRediT authorship contribution statement

Maria Emerla: Conceptualization, Methodology, Investigation, Data curation, Writing – original draft.

Piotr Bazarnik: Conceptualization, Methodology, Investigation, Data curation, Writing – review & editing, Project administration, Funding acquisition.

Yi Huang: Investigation, Validation, Writing – review & editing.

Anita Wojciechowska: Investigation.

Marta Ciemiorek Bartkowska: Investigation.

Monika Wieczorek-Czarnocka: Investigation.

Purbayanto Muhammad Abiyyu Kenichi: Investigation.

Jaroslaw Pura: Investigation.

Agnieszka Jastrzębska: Writing – review & editing

M. Lewandowska: Conceptualization, Writing – review & editing

T.G. Langdon: Conceptualization, Supervision, Writing – review & editing

Declaration of competing interest

The authors declare that they have no known competing financial interests or personal relationships that could have appeared to influence the work reported in this paper.

Acknowledgments

Data availability

Data will be made available on request.

References

[1] R.Z. Valiev, I. V. Alexandrov, M. Kawasaki, T.G. Langdon, Ultrafine-Grained Materials, in: Miner. Met. Mater. Ser., Springer Nature, Cham, Switzerland, 2024: pp. 1–29. https://doi.org/10.1007/978-3-031-31729-3_1.

[2] T.G.Langdon. R. Z. Valiev, Al. P. Zhilyaev, Bulk Nanostructured Materials: Fundamentals and Applications, John Wiley & Sons, Inc., Hoboken, New Jersey, USA, 2013. https://doi.org/10.1142/9789814397988_0011.

[3] R.Z. Valiev, Y. Estrin, Z. Horita, T.G. Langdon, M.J. Zehetbauer, Y.T. Zhu, Fundamentals of superior properties in bulk NanoSPD materials, Mater. Res. Lett. 4 (2016) 1–21. https://doi.org/10.1080/21663831.2015.1060543.

[4] A.P. Zhilyaev, T.G. Langdon, Using high-pressure torsion for metal processing: Fundamentals and applications, Prog. Mater. Sci. 53 (2008) 893–979. https://doi.org/10.1016/j.pmatsci.2008.03.002.

[5] E.O. Hall, The deformation and ageing of mild steel III discussion of results, Proc. Phys. Soc. Sect. B. 64 (1951) 747–753.

[6] N.J. Petch, The cleavage strength of polycrystals, J. Iron Steel Inst. 174 (1953) 25–28.

[7] K. Edalati, A.Q. Ahmed, S. Akrami, K. Ameyama, V. Aptukov, R.N. Asfandiyarov, M. Ashida, V. Astanin, A. Bachmaier, V. Beloshenko, E. V. Bobruk, K. Bryła, J.M. Cabrera, A.P. Carvalho, N.Q. Chinh, I.C. Choi, R. Chulist, J.M. Cubero-Sesin, G. Davdian, M. Demirtas, S. Divinski, K. Durst, J. Dvorak, P. Edalati, S. Emura, N.A. Enikeev, G. Faraji, R.B. Figueiredo, R. Floriano, M. Fouladvind, D. Fruchart, M. Fuji, H. Fujiwara, M. Gajdics, D. Gheorghe, L. Gondek, J.E. González-Hernández, A. Gornakova, T. Grosdidier, J. Gubicza, D. Gunderov, L. He, O.F. Higuera, S. Hirosawa, A. Hohenwarter, Z. Horita, J. Horky, Y. Huang, J. Huot, Y. Ikoma, T. Ishihara, Y. Ivanisenko, J. il Jang, A.M. Jorge, M. Kawabata-Ota, M. Kawasaki, T. Khelfa, J. Kobayashi, L. Kommel, A. Korneva, P. Kral, N. Kudriashova, S. Kuramoto, T.G. Langdon, D.H. Lee, V.I. Levitas, C. Li, H.W. Li, Y. Li, Z. Li, H.J. Lin, K.D. Liss, Y. Liu, D.M.M. Cardona, K. Matsuda, A. Mazilkin, Y. Mine, H. Miyamoto, S.C. Moon, T. Müller, J.A. Muñoz, M.Y. Murashkin, M. Naeem, M. Novelli, D. Olasz, R. Pippan, V. V. Popov, E.N. Popova, G. Purcek, P. de Rango, O. Renk, D. Retraint, Á. Révész, V. Roche, P. Rodriguez-Calvillo, L. Romero-Resendiz, X. Sauvage, T. Sawaguchi, H. Sena, H. Shahmir, X. Shi, V. Sklenicka, W. Skrotzki, N. Skryabina, F. Staab, B. Straumal, Z. Sun, M. Szczerba, Y. Takizawa, Y. Tang, R.Z. Valiev, A. Vozniak, A. Voznyak, B. Wang, J.T. Wang, G. Wilde, F. Zhang, M. Zhang, P. Zhang, J. Zhou, X. Zhu, Y.T. Zhu, Severe plastic deformation for producing superfunctional ultrafine-grained and heterostructured materials: An interdisciplinary review, J. Alloys Compd. 1002 (2024). https://doi.org/10.1016/j.jallcom.2024.174667.

[8] K. Edalati, A. Bachmaier, V.A. Beloshenko, Y. Beygelzimer, V.D. Blank, W.J. Botta, K. Bryła, J. Čížek, S. Divinski, N.A. Enikeev, Y. Estrin, G. Faraji, R.B. Figueiredo, M. Fuji, T. Furuta, T. Grosdidier, J. Gubicza, A. Hohenwarter, Z. Horita, J. Huot, Y. Ikoma, M. Janeček, M. Kawasaki, P. Král, S. Kuramoto, T.G. Langdon, D.R. Leiva, V.I. Levitas, A. Mazilkin, M. Mito, H. Miyamoto, T. Nishizaki, R. Pippan, V. V. Popov, E.N. Popova, G. Purcek, O. Renk, Á. Révész, X. Sauvage, V. Sklenicka, W. Skrotzki, B.B. Straumal, S. Suwas, L.S. Toth, N. Tsuji, R.Z. Valiev, G. Wilde, M.J. Zehetbauer, X. Zhu, Nanomaterials by severe plastic deformation: review of historical developments and recent advances, Mater. Res. Lett. 10 (2022) 163–256. https://doi.org/10.1080/21663831.2022.2029779.

[9] R.Z. Valiev, Y. Estrin, Z. Horita, T.G. Langdon, M.J. Zehetbauer, Y. Zhu, Producing Bulk Ultrafine-Grained Materials by Severe Plastic Deformation: Ten Years Later, Jom. 68 (2006) 1216–1226. https://doi.org/10.1007/s11837-016-1820-6.

[10] P. Bazarnik, Y. Huang, M. Lewandowska, T.G. Langdon, Enhanced grain refinement and microhardness by hybrid processing using hydrostatic extrusion and high-pressure torsion, Mater. Sci. Eng. A. 712 (2018) 513–520. https://doi.org/10.1016/j.msea.2017.12.007.

[11] M. Kawasaki, Z. Horita, T.G. Langdon, Microstructural evolution in high purity aluminum

processed by ECAP, Mater. Sci. Eng. A. 524 (2009) 143–150. https://doi.org/10.1016/j.msea.2009.06.032.

[12] J.J. Jonas, C. Ghosh, L.S. Toth, The equivalent strain in high pressure torsion, Mater. Sci. Eng. A. 607 (2014) 530–535. https://doi.org/10.1016/j.msea.2014.04.046.

[13] V. V. Popov, E.N. Popova, A. V. Stolbovskiy, Nanostructuring Nb by various techniques of severe plastic deformation, Mater. Sci. Eng. A. 539 (2012) 22–29. https://doi.org/10.1016/j.msea.2011.12.082.

[14] T. Hebesberger, H.P. Stüwe, A. Vorhauer, F. Wetscher, R. Pippan, Structure of Cu deformed by high pressure torsion, Acta Mater. 53 (2005) 393–402. https://doi.org/10.1016/j.actamat.2004.09.043.

[15] P. Král, J. Staněk, L. Kunčická, F. Seitl, L. Petrich, V. Schmidt, V. Beneš, V. Sklenička, Microstructure changes in HPT-processed copper occurring at room temperature, Mater. Charact. 151 (2019) 602–611. https://doi.org/10.1016/j.matchar.2019.03.046.

[16] S. Sabbaghianrad, T.G. Langdon, Microstructural saturation, hardness stability and superplasticity in ultrafine-grained metals processed by a combination of severe plastic deformation techniques, Lett. Mater. 5 (2015) 335–340. https://doi.org/10.22226/2410-3535-2015-3-335-340.

[17] S. Sabbaghianrad, T.G. Langdon, An evaluation of the saturation hardness in an ultrafine-grained aluminum 7075 alloy processed using different techniques, J. Mater. Sci. 50 (2015) 4357–4365. https://doi.org/10.1007/s10853-015-8989-x.

[18] S. Sabbaghianrad, J. Wongsa-Ngam, M. Kawasaki, T.G. Langdon, An examination of the saturation microstructures achieved in ultrafine-grained metals processed by high-pressure torsion, J. Mater. Res. Technol. 3 (2014) 319–326. https://doi.org/10.1016/j.jmrt.2014.10.002.

[19] P. Jenei, E.Y. Yoon, J. Gubicza, H.S. Kim, J.L. Lábár, T. Ungár, Microstructure and hardness of copper-carbon nanotube composites consolidated by High Pressure Torsion, Mater. Sci. Eng. A. 528 (2011) 4690–4695. https://doi.org/10.1016/j.msea.2011.02.066.

[20] A. Dhal, B. Prathyusha, R. Kumar, S.K. Panigrahi, Twin evolution and work-hardening phenomenon of a bulk ultrafine grained copper with high thermal stability and strength-ductility synergy, Mater. Sci. Eng. A. 802 (2021) 140622. https://doi.org/10.1016/j.msea.2020.140622.

[21] H. Jiang, Y.T. Zhu, D.P. Butt, I. V. Alexandrov, T.C. Lowe, Microstructural evolution, microhardness and thermal stability of HPT-processed Cu, Mater. Sci. Eng. A. 290 (2000) 128–138. https://doi.org/10.1016/S0921-5093(00)00919-9.

[22] R.K. Islamgaliev, F. Chmelik, R. Kuzel, Thermal structure changes in copper and nickel processed by severe plastic deformation, Mater. Sci. Eng. A. 234–236 (1997) 335–338. https://doi.org/10.1016/s0921-5093(97)00247-5.

[23] D. Zhou, D. Zhang, C. Kong, P. Munroe, R. Torrens, Grain and nanoparticle coarsening of an ultrafine structured Cu-5 vol.%Al2O3 nanocomposite during isochronal annealing, J. Alloys Compd. 642 (2015) 83–91. https://doi.org/10.1016/j.jallcom.2015.04.106.

[24] B. Tian, P. Liu, K. Song, Y. Li, Y. Liu, F. Ren, J. Su, Microstructure and properties at elevated temperature of a nano-Al2O3 particles dispersion-strengthened copper base composite, Mater. Sci. Eng. A. 435–436 (2006) 705–710. https://doi.org/10.1016/j.msea.2006.07.129.

[25] J. Naser, H. Ferkel, W. Riehemann, Grain stabilisation of copper with nanoscaled Al2O3-powder, Mater. Sci. Eng. A. 234–236 (1997) 470–473. https://doi.org/10.1016/s0921-5093(97)00263-3.

[26] M. Emerla, P. Bazarnik, Y. Huang, M. Lewandowska, T.G. Langdon, Using direct high-pressure torsion synthesis to produce aluminium matrix nanocomposites reinforced with carbon nanotubes, J. Alloys Compd. 968 (2023). https://doi.org/10.1016/j.jallcom.2023.171928.

[27] J. Lipecka, M. Andrzejczuk, M. Lewandowska, J. Janczak-Rusch, K.J. Kurzydłowski, Evaluation of thermal stability of ultrafine grained aluminium matrix composites reinforced with

carbon nanotubes, Compos. Sci. Technol. 71 (2011) 1881–1885. https://doi.org/10.1016/j.compscitech.2011.09.001.

[28] M. Jahedi, M.H. Paydar, M. Knezevic, Enhanced microstructural homogeneity in metal-matrix composites developed under high-pressure-double-torsion, Mater. Charact. 104 (2015) 92–100. https://doi.org/10.1016/j.matchar.2015.04.012.

[29] M.I. Abd El Aal, Effect of high-pressure torsion processing on the microstructure evolution and mechanical properties of consolidated micro size Cu and Cu-SiC powders, Adv. Powder Technol. 28 (2017) 2135–2150. https://doi.org/10.1016/j.apt.2017.05.020.

[30] D. Shen, P. Gao, Y. He, J. Gong, J. Du, A Cu-Al2O3 Composite with Ultrahigh Tensile Strength Prepared by High-Pressure Torsion, J. Mater. Eng. Perform. (2022) 1–6. https://doi.org/10.1007/s11665-022-06936-9.

[31] K. Edalati, M. Ashida, Z. Horita, T. Matsui, H. Kato, Wear resistance and tribological features of pure aluminum and Al-Al2O3 composites consolidated by high-pressure torsion, Wear. 310 (2014) 83–89. https://doi.org/10.1016/j.wear.2013.12.022.

[32] P. Bazarnik, S. Nosewicz, B. Romelczyk-Baishya, M. Chmielewski, A. Strojny Nędza, J. Maj, Y. Huang, M. Lewandowska, T.G. Langdon, Effect of spark plasma sintering and high-pressure torsion on the microstructural and mechanical properties of a Cu–SiC composite, Mater. Sci. Eng. A. 766 (2019). https://doi.org/10.1016/j.msea.2019.138350.

[33] T. Tokunaga, K. Kaneko, K. Sato, Z. Horita, Microstructure and mechanical properties of aluminum-fullerene composite fabricated by high pressure torsion, Scr. Mater. 58 (2008) 735–738. https://doi.org/10.1016/j.scriptamat.2007.12.010.

[34] D.D. Phuong, P. Van Trinh, N. Van An, N. Van Luan, P.N. Minh, R.K. Khisamov, K.S. Nazarov, L.R. Zubairov, R.R. Mulyukov, A.A. Nazarov, Effects of carbon nanotube content and annealing temperature on the hardness of CNT reinforced aluminum nanocomposites processed by the high pressure torsion technique, J. Alloys Compd. 613 (2014) 68–73. https://doi.org/10.1016/j.jallcom.2014.05.219.

[35] G. Korznikova, T. Czeppe, G. Khalikova, D. Gunderov, E. Korznikova, L. Litynska-Dobrzynska, M. Szlezynger, Microstructure and mechanical properties of Cu-graphene composites produced by two high pressure torsion procedures, Mater. Charact. 161 (2020) 110122. https://doi.org/10.1016/j.matchar.2020.110122.

[36] Y. Huang, P. Bazarnik, D. Wan, D. Luo, P.H.R. Pereira, M. Lewandowska, J. Yao, B.E. Hayden, T.G. Langdon, The fabrication of graphene-reinforced Al-based nanocomposites using high-pressure torsion, Acta Mater. 164 (2019) 499–511. https://doi.org/10.1016/j.actamat.2018.10.060.

[37] Z. ZHENG, X. xia YANG, J. chao LI, X. xi ZHANG, I. MUHAMMAD, L. GENG, Preparation and properties of graphene nanoplatelets reinforced aluminum composites, Trans. Nonferrous Met. Soc. China (English Ed. 31 (2021) 878–886. https://doi.org/10.1016/S1003-6326(21)65546-2.

[38] N. Khobragade, K. Sikdar, B. Kumar, S. Bera, D. Roy, Mechanical and electrical properties of copper-graphene nanocomposite fabricated by high pressure torsion, J. Alloys Compd. 776 (2019) 123–132. https://doi.org/10.1016/j.jallcom.2018.10.139.

[39] P. Hidalgo-Manrique, X. Lei, R. Xu, M. Zhou, I.A. Kinloch, R.J. Young, Copper/graphene composites: a review, J. Mater. Sci. 54 (2019) 12236–12289. https://doi.org/10.1007/s10853-019-03703-5.

[40] A.P. Zhilyaev, I. Shakhova, A. Belyakov, R. Kaibyshev, T.G. Langdon, Wear resistance and electroconductivity in copper processed by severe plastic deformation, Wear. 305 (2013) 89–99. https://doi.org/10.1016/j.wear.2013.06.001.

[41] A.P. Zhilyaev, I. Shakhova, A. Belyakov, R. Kaibyshev, T.G. Langdon, Effect of annealing on wear resistance and electroconductivity of copper processed by high-pressure torsion, J. Mater. Sci. 49 (2014) 2270–2278. https://doi.org/10.1007/s10853-013-7923-3.

[42] G. Giovannetti, P.A. Khomyakov, G. Brocks, V.M. Karpan, J. Van Den Brink, P.J. Kelly, Doping

graphene with metal contacts, Phys. Rev. Lett. 101 (2008) 4–7. https://doi.org/10.1103/PhysRevLett.101.026803.

[43] P.A. Khomyakov, G. Giovannetti, P.C. Rusu, G. Brocks, J. Van Den Brink, P.J. Kelly, First-principles study of the interaction and charge transfer between graphene and metals, Phys. Rev. B - Condens. Matter Mater. Phys. 79 (2009) 1–12. https://doi.org/10.1103/PhysRevB.79.195425.

[44] L. Zhang, E. Pollak, W.C. Wang, P. Jiang, P.A. Glans, Y. Zhang, J. Cabana, R. Kostecki, C. Chang, M. Salmeron, J. Zhu, J. Guo, Electronic structure study of ordering and interfacial interaction in graphene/Cu composites, Carbon N. Y. 50 (2012) 5316–5322. https://doi.org/10.1016/j.carbon.2012.07.020.

[45] N. Kurantowicz, E. Sawosz, S. Jaworski, M. Kutwin, B. Strojny, M. Wierzbicki, J. Szeliga, A. Hotowy, L. Lipińska, R. Koziński, J. Jagiełło, A. Chwalibog, Interaction of graphene family materials with Listeria monocytogenes and Salmonella enterica, Nanoscale Res. Lett. 10 (2015) 1–12. https://doi.org/10.1186/s11671-015-0749-y.

[46] C. Xu, Z. Horita, T.G. Langdon, The evolution of homogeneity in an aluminum alloy processed using high-pressure torsion, Acta Mater. 56 (2008) 5168–5176. https://doi.org/10.1016/j.actamat.2008.06.036.

[47] K. Edalati, Z. Horita, T.G. Langdon, The significance of slippage in processing by high-pressure torsion, Scr. Mater. 60 (2009) 9–12. https://doi.org/10.1016/j.scriptamat.2008.08.042.

[48] P.H.R. Pereira, R.B. Figueiredo, Y. Huang, P.R. Cetlin, T.G. Langdon, Modeling the temperature rise in high-pressure torsion, Mater. Sci. Eng. A. 593 (2014) 185–188. https://doi.org/10.1016/j.msea.2013.11.015.

[49] K. Edalati, Y. Hashiguchi, P.H.R. Pereira, Z. Horita, T.G. Langdon, Effect of temperature rise on microstructural evolution during high-pressure torsion, Mater. Sci. Eng. A. 714 (2018) 167–171. https://doi.org/10.1016/j.msea.2017.12.095.

[50] J. Chen, C. Li, W. Cao, S. Sang, Q. Wu, H. Liu, K. Liu, Conductive and high anticorrosive rGO-modified copper foil prepared by electrocoagulation and chemical reduction, Ionics (Kiel). 25 (2019) 2935–2944. https://doi.org/10.1007/s11581-018-2702-4.

[51] V.B. Mohan, R. Brown, K. Jayaraman, D. Bhattacharyya, Characterisation of reduced graphene oxide: Effects of reduction variables on electrical conductivity, Mater. Sci. Eng. B. 193 (2015) 49–60. https://doi.org/10.1016/j.mseb.2014.11.002.

[52] J. Bin Wu, M.L. Lin, X. Cong, H.N. Liu, P.H. Tan, Raman spectroscopy of graphene-based materials and its applications in related devices, Chem. Soc. Rev. 47 (2018) 1822–1873. https://doi.org/10.1039/c6cs00915h.

[53] A.C. Ferrari, Raman spectroscopy of graphene and graphite: Disorder, electron-phonon coupling, doping and nonadiabatic effects, Solid State Commun. 143 (2007) 47–57. https://doi.org/10.1016/j.ssc.2007.03.052.

[54] K.N. Kudin, B. Ozbas, H.C. Schniepp, R.K. Prud'homme, I.A. Aksay, R. Car, Raman spectra of graphite oxide and functionalized graphene sheets, Nano Lett. 8 (2008) 36–41. https://doi.org/10.1021/nl071822y.

[55] J. Song, L. Xu, C. Zhou, R. Xing, Q. Dai, D. Liu, H. Song, Synthesis of graphene oxide based cuo nanoparticles composite electrode for highly enhanced nonenzymatic glucose detection, ACS Appl. Mater. Interfaces. 5 (2013) 12928–12934. https://doi.org/10.1021/am403508f.

[56] I. Sengupta, S.S.S. Sharat Kumar, S.K. Pal, S. Chakraborty, Characterization of structural transformation of graphene oxide to reduced graphene oxide during thermal annealing, J. Mater. Res. 35 (2020) 1197–1204. https://doi.org/10.1557/jmr.2020.55.

[57] J. Li, H. Ding, B. Li, L. Wang, Microstructure evolution and properties of a Cu–Cr–Zr alloy with high strength and high conductivity, Mater. Sci. Eng. A. 819 (2021). https://doi.org/10.1016/j.msea.2021.141464.

[58] P. Jenei, J. Gubicza, E.Y. Yoon, H.S. Kim, J.L. Lábár, High temperature thermal stability of pure copper and copper-carbon nanotube composites consolidated by High Pressure Torsion, Compos. Part A Appl. Sci. Manuf. 51 (2013) 71–79. https://doi.org/10.1016/j.compositesa.2013.04.007.

[59] M. Darabi, M. Rajabi, B. Junipour, M.T. Noghani, The effect of sintering temperature on Cu-Cnts nano composites properties produced by pm method, Sci. Sinter. 50 (2018) 477–486. https://doi.org/10.2298/SOS1804477D.

[60] N. Wang, Y. Wen, L.Q. Chen, Pinning force from multiple second-phase particles in grain growth, Comput. Mater. Sci. 93 (2014) 81–85. https://doi.org/10.1016/j.commatsci.2014.06.030.

[61] Z. Li, J. Wang, H. Huang, Influences of grain/particle interfacial energies on second-phase particle pinning grain coarsening of polycrystalline, J. Alloys Compd. 818 (2020). https://doi.org/10.1016/j.jallcom.2019.152848.

[62] S. Dangwal, K. Edalati, R.Z. Valiev, T.G. Langdon, Breaks in the Hall–Petch Relationship after Severe Plastic Deformation of Magnesium, Aluminum, Copper, and Iron, Crystals. 13 (2023) 413. https://doi.org/10.3390/cryst13030413.

[63] F. Ternero, L.G. Rosa, P. Urban, J.M. Montes, F.G. Cuevas, Influence of the total porosity on the properties of sintered materials—a review, Metals (Basel). 11 (2021). https://doi.org/10.3390/met11050730.

[64] T. Kaiser, G. Dehm, C. Kirchlechner, A. Menzel, H. Bishara, Probing porosity in metals by electrical conductivity: Nanoscale experiments and multiscale simulations, Eur. J. Mech. A/Solids. 97 (2023) 104777. https://doi.org/10.1016/j.euromechsol.2022.104777.

[65] M.I. Abd El Aal, Wear properties of copper and copper composites powders consolidated by high-pressure torsion, Friction. 8 (2020) 433–450. https://doi.org/10.1007/s40544-019-0285-3.

[66] F.A. Sadykov, N.P. Barykin, I.R. Aslanyan, The influence of strain-heat processing on copper wear, Wear. 212 (1997) 160–164. https://doi.org/10.1016/S0043-1648(97)00164-6.

[67] Z. Zhang, S. Hosoda, I.S. Kim, Y. Watanabe, Grain refining performance for Al and Al-Si alloy casts by addition of equal-channel angular pressed Al-5 mass% Ti alloy, Mater. Sci. Eng. A. 425 (2006) 55–63. https://doi.org/10.1016/j.msea.2006.03.018.

[68] M. Chegini, A. Fallahi, M.H. Shaeri, Effect of Equal Channel Angular Pressing (ECAP) on Wear Behavior of Al-7075 Alloy, Procedia Mater. Sci. 11 (2015) 95–100. https://doi.org/10.1016/j.mspro.2015.11.116.

[69] C.T. Wang, N. Gao, R.J.K. Wood, T.G. Langdon, Wear behavior of an aluminum alloy processed by equal-channel angular pressing, J. Mater. Sci. 46 (2011) 123–130. https://doi.org/10.1007/s10853-010-4862-0.

[70] H. Garbacz, M. Gradzka-Dahlke, K.J. Kurzydłowski, The tribological properties of nano-titanium obtained by hydrostatic extrusion, Wear. 263 (2007) 572–578. https://doi.org/10.1016/j.wear.2006.11.047.

[71] N. Gao, C.T. Wang, R.J.K. Wood, T.G. Langdon, Wear resistance of SPD-processed alloys, Mater. Sci. Forum. 667–669 (2011) 1095–1100. https://doi.org/10.4028/www.scientific.net/MSF.667-669.1095.

[72] N. Gao, C.T. Wang, R.J.K. Wood, T.G. Langdon, Tribological properties of ultrafine-grained materials processed by severe plastic deformation, J. Mater. Sci. 47 (2012) 4779–4797. https://doi.org/10.1007/s10853-011-6231-z.

[73] P.A. Manohar, M. Ferry, T. Chandra, Five Decades of the Zener Equation, ISIJ Int. 38 (1998) 913–924. https://doi.org/10.2355/isijinternational.38.913.

[74] S. Suárez, E. Ramos-Moore, B. Lechthaler, F. Mücklich, Grain growth analysis of multiwalled carbon nanotube-reinforced bulk Ni composites, Carbon N. Y. 70 (2014) 173–178. https://doi.org/10.1016/j.carbon.2013.12.089.

[75] K. Edalati, J.M. Cubero-Sesin, A. Alhamidi, I.F. Mohamed, Z. Horita, Influence of severe plastic deformation at cryogenic temperature on grain refinement and softening of pure metals: Investigation using high-pressure torsion, Mater. Sci. Eng. A. 613 (2014) 103–110. https://doi.org/10.1016/j.msea.2014.06.084.

[76] K. Raidongia, A.T.L. Tan, J. Huang, Graphene Oxide: Some New Insights into an Old Material, Second Edi, Elsevier Ltd, 2014. https://doi.org/10.1016/B978-0-08-098232-8.00014-0.

[77] S.H. Huh, Thermal Reduction of Graphene Oxide, Phys. Appl. Graphene - Exp. (2011) 73–90.

[78] L. Hu, A. Wang, W. Wang, Structural Evolution of Graphene Oxide and Its Thermal Stability During High Temperature Sintering, J. Wuhan Univ. Technol. Mater. Sci. Ed. 37 (2022) 342–349. https://doi.org/10.1007/s11595-022-2537-8.

[79] T. Szabó, O. Berkesi, P. Forgó, K. Josepovits, Y. Sanakis, D. Petridis, I. Dékány, Evolution of surface functional groups in a series of progressively oxidized graphite oxides, Chem. Mater. 18 (2006) 2740–2749. https://doi.org/10.1021/cm060258+.

[80] A. Lerf, H. He, M. Forster, J. Klinowski, Structure of graphite oxide revisited, J. Phys. Chem. B. 102 (1998) 4477–4482. https://doi.org/10.1021/jp9731821.

[81] I. Sengupta, S. Chakraborty, M. Talukdar, S.K. Pal, S. Chakraborty, Thermal reduction of graphene oxide: How temperature influences purity, J. Mater. Res. 33 (2018) 4113–4122. https://doi.org/10.1557/jmr.2018.338.

[82] H.C. Schniepp, J.L. Li, M.J. McAllister, H. Sai, M. Herrera-Alonson, D.H. Adamson, R.K. Prud'homme, R. Car, D.A. Seville, I.A. Aksay, Functionalized single graphene sheets derived from splitting graphite oxide, J. Phys. Chem. B. 110 (2006) 8535–8539. https://doi.org/10.1021/jp060936f.

List of illustrations

List of tables

Sample	Friction coeficient	Wear rate mm3/N*m	Mass reduction mg
Cu SPS	0.73	4.49 x 10^{-4}	25
Cu HPT	0.72	2.62 x 10^{-4}	28
Cu-GO HPT	0.80	3.89 x 10^{-4}	32

	C-K	O-K	Cu-K
Point 1	14.3	43.4	45.3
Point 2	2.5	33.2	64.3
Point 3	0.9	3.4	95.7
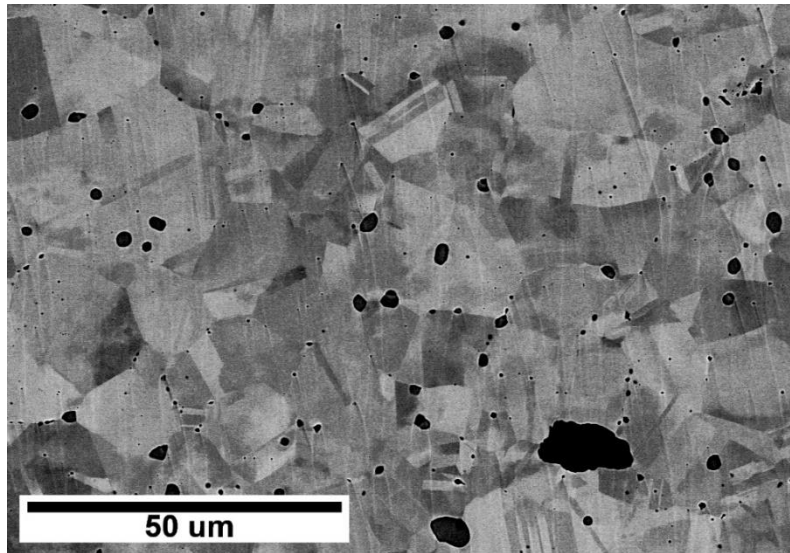
Figure 1 SEM BSE image of microstructure of Cu SPS
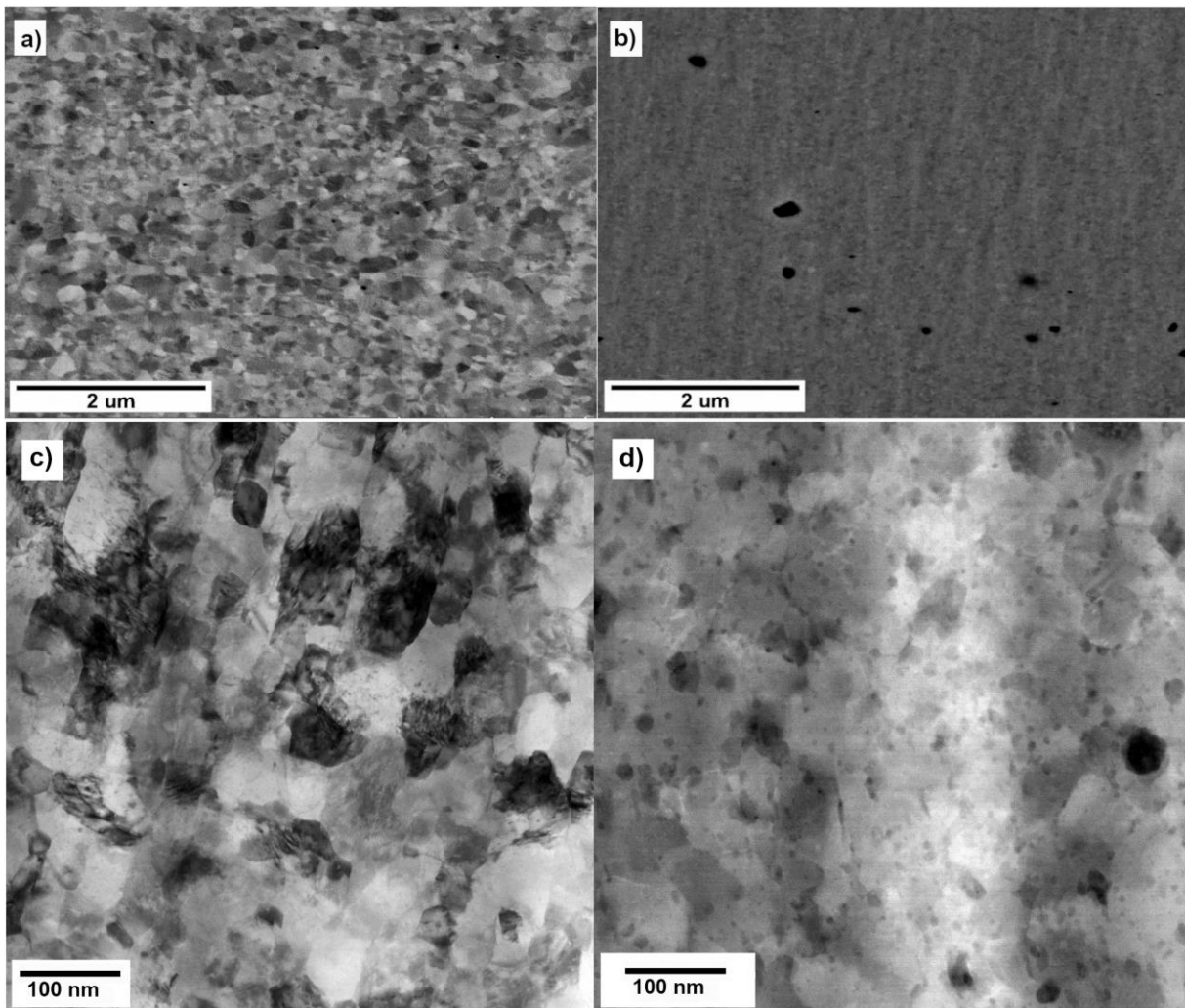
Figure 2 a) SEM BSE image of Cu after HPT; b) SEM BSE image of Cu-GO after HPT; c) STEM image of Cu-GO in bright-field (BF) and d) STEM image of Cu-GO in high-angle annular dark field (HAADF) mode
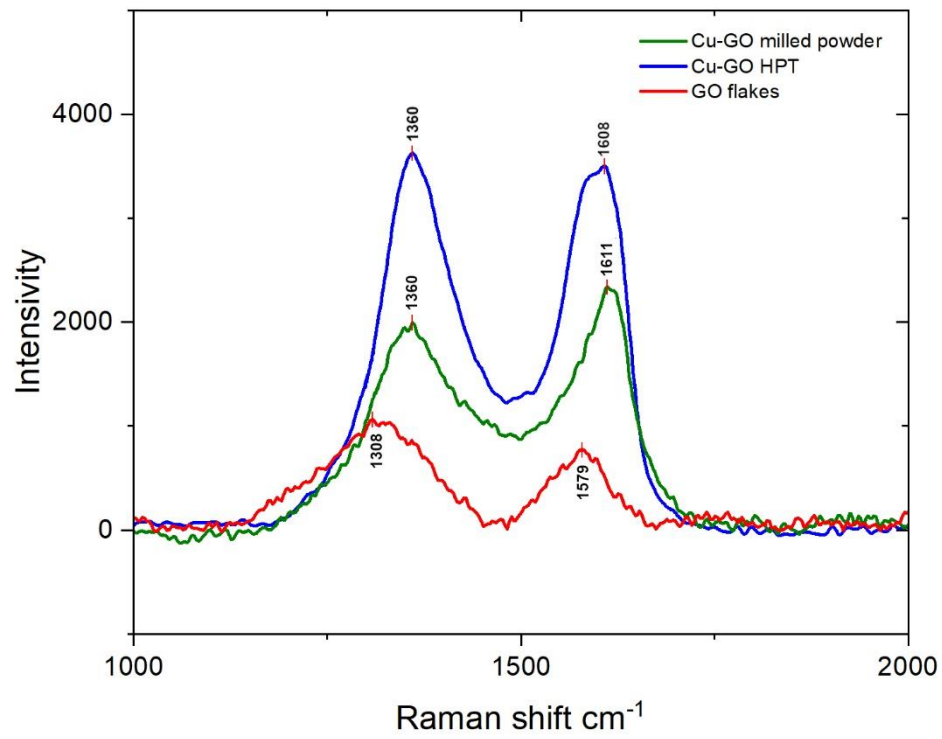
Figure 3 Raman spectra of: GO flakes, powder mixture of GO and Cu after mechanical milling, and Cu-GO HPT nanocomposite
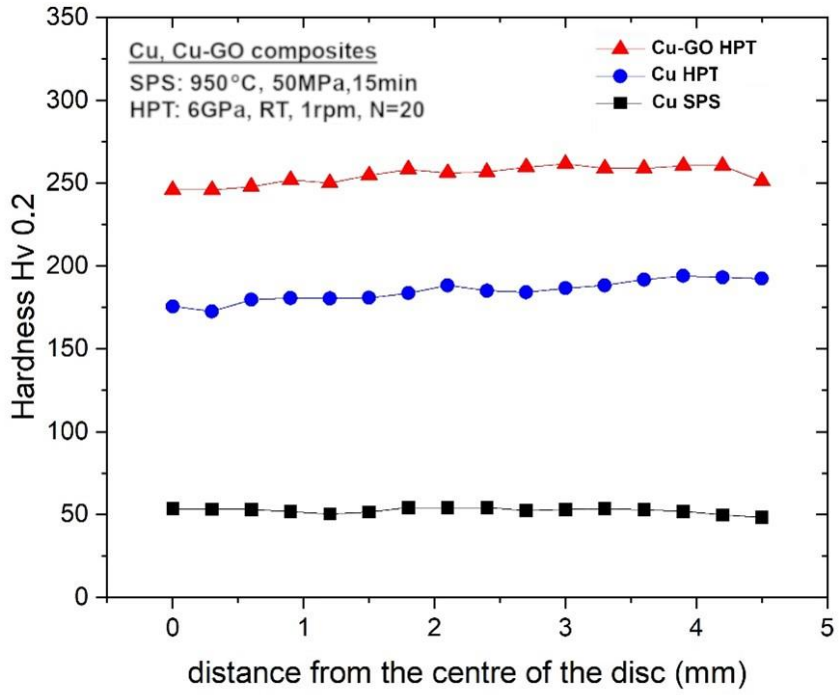
Figure 4 Hardness of the samples (Cu SPS, Cu HPT, and Cu-GO HPT) in the function of distance from disc centre
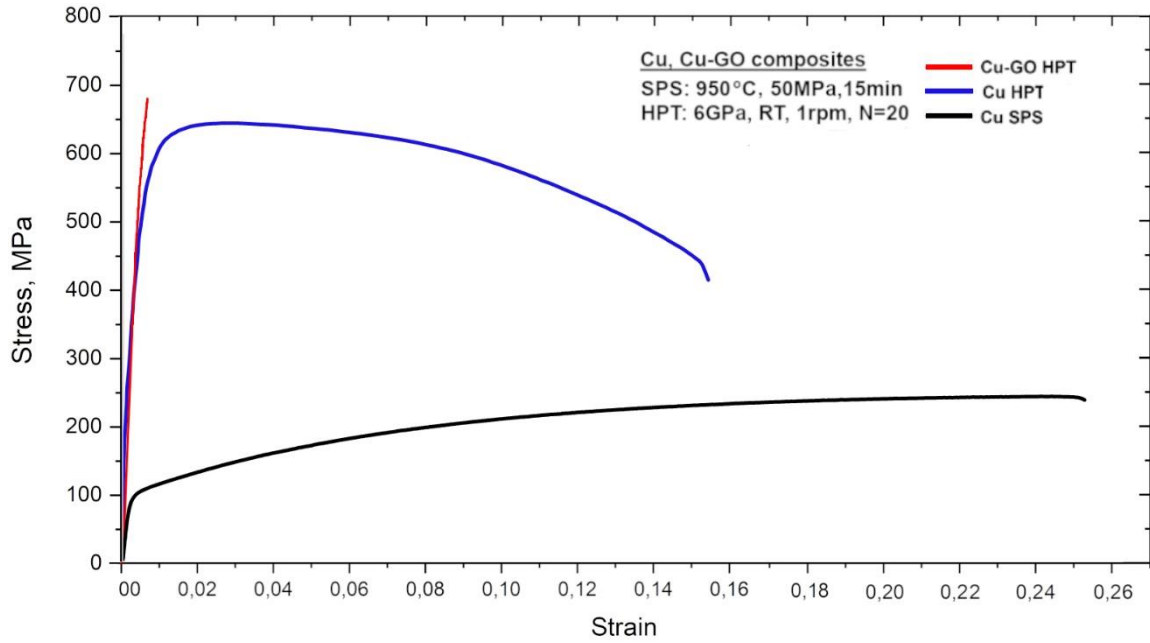
Figure 5 Tensile strength curves of Cu SPS, Cu HPT and Cu-GO HPT
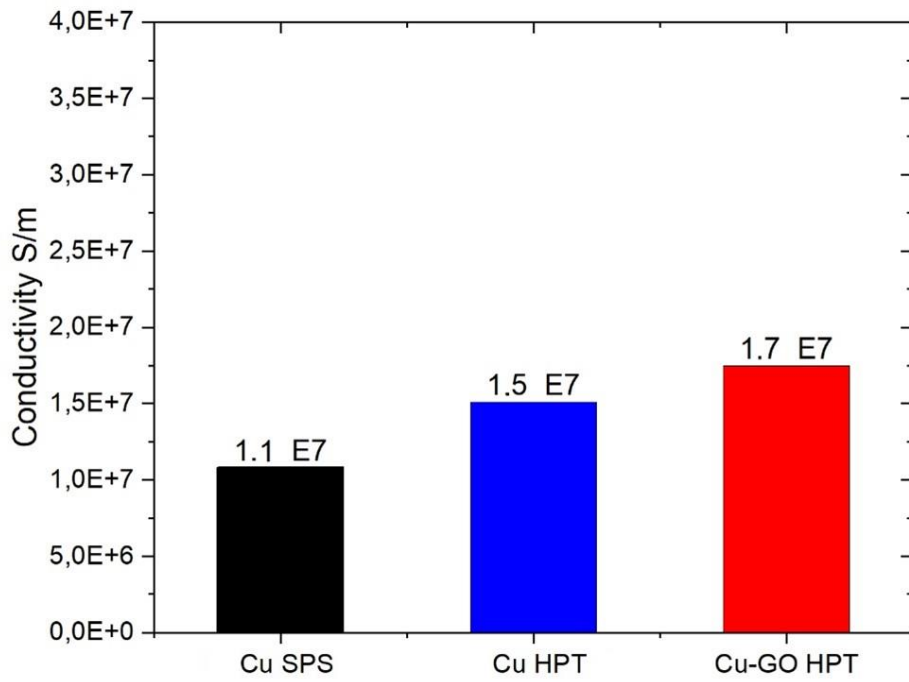
Figure 6 Electrical conductivity of tested samples (Cu SPS, Cu HPT, and Cu-GO HPT)
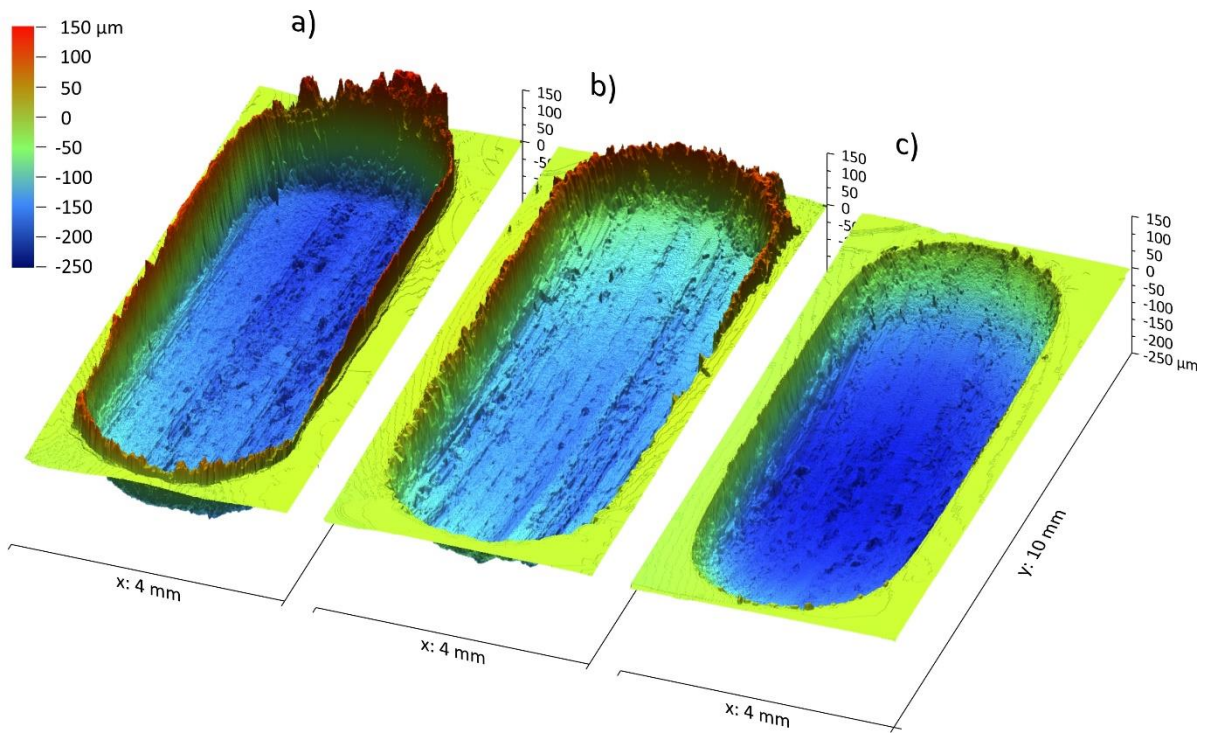
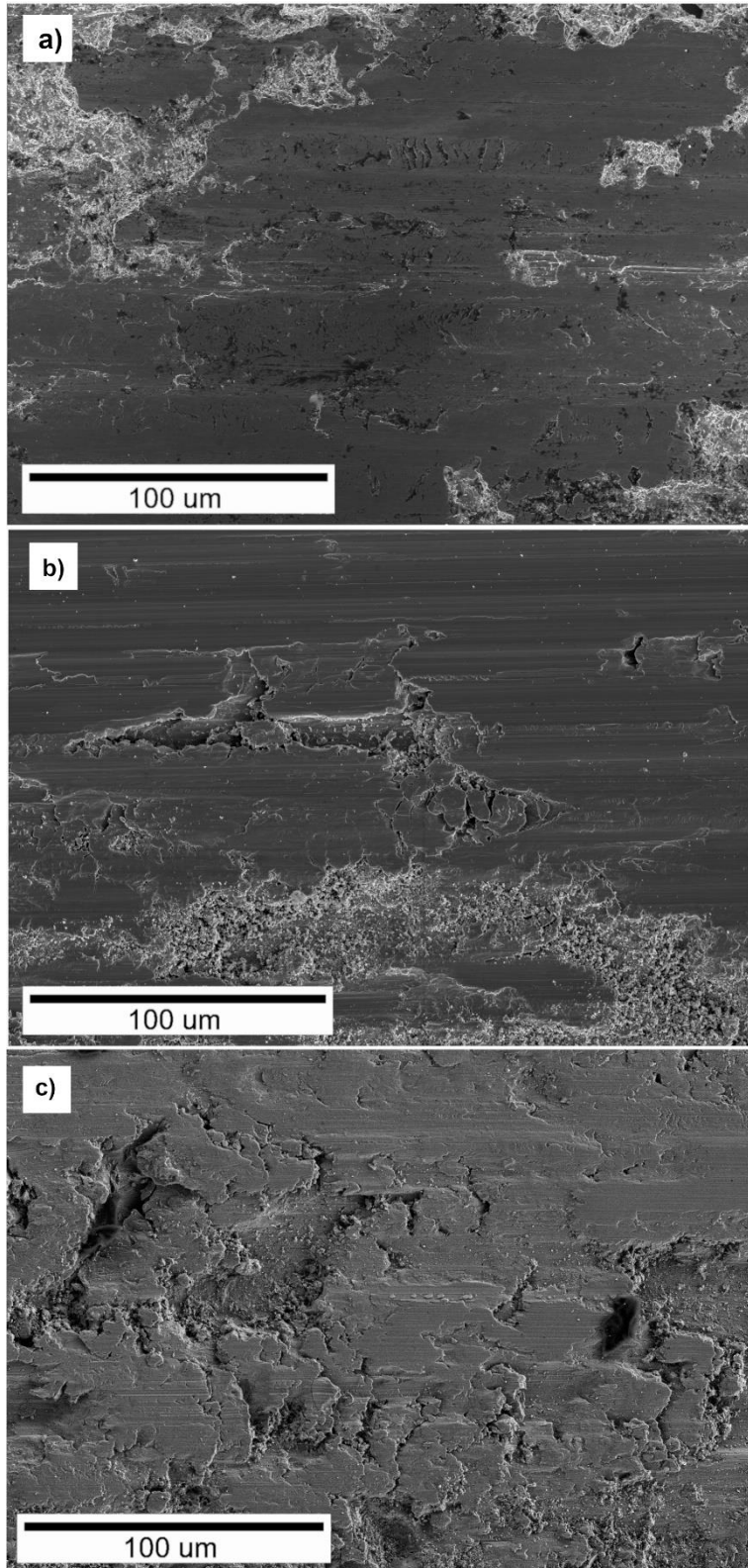*Figure 7 Profilometry images of the tested materials a) Cu SPS; b) Cu HPT; c) Cu-GO HPT*

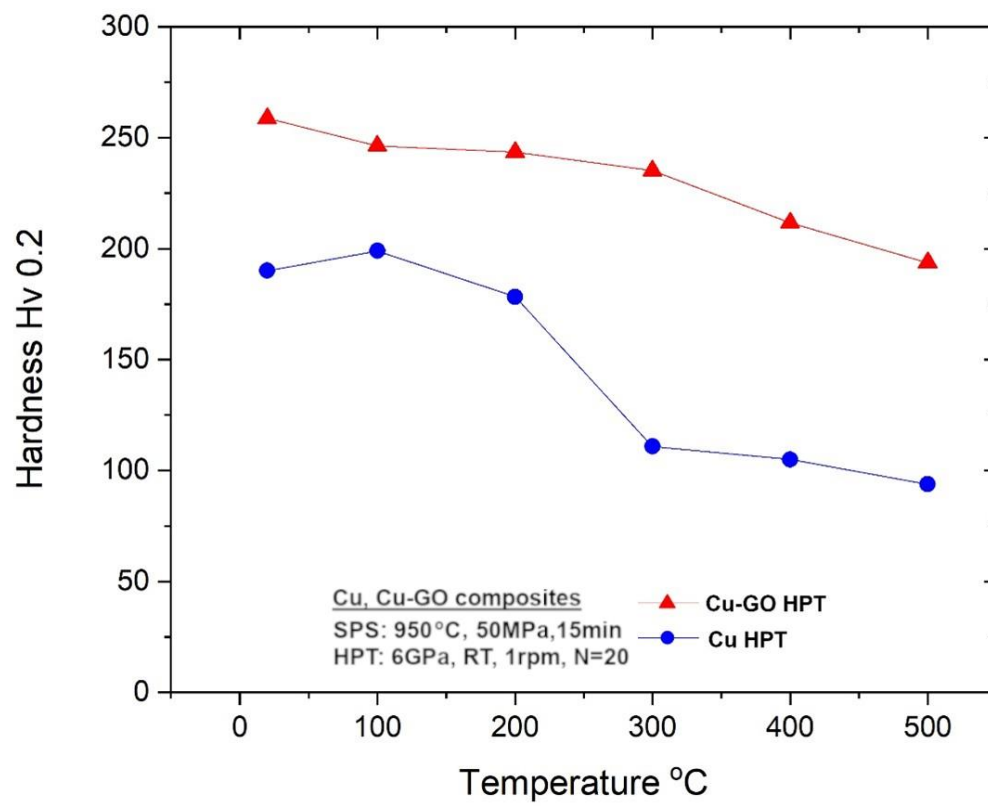*Figure 8 Surface after wear sliding test in SEM SE image: a) Cu SPS; b) Cu HPT; c) Cu-GO HPT*

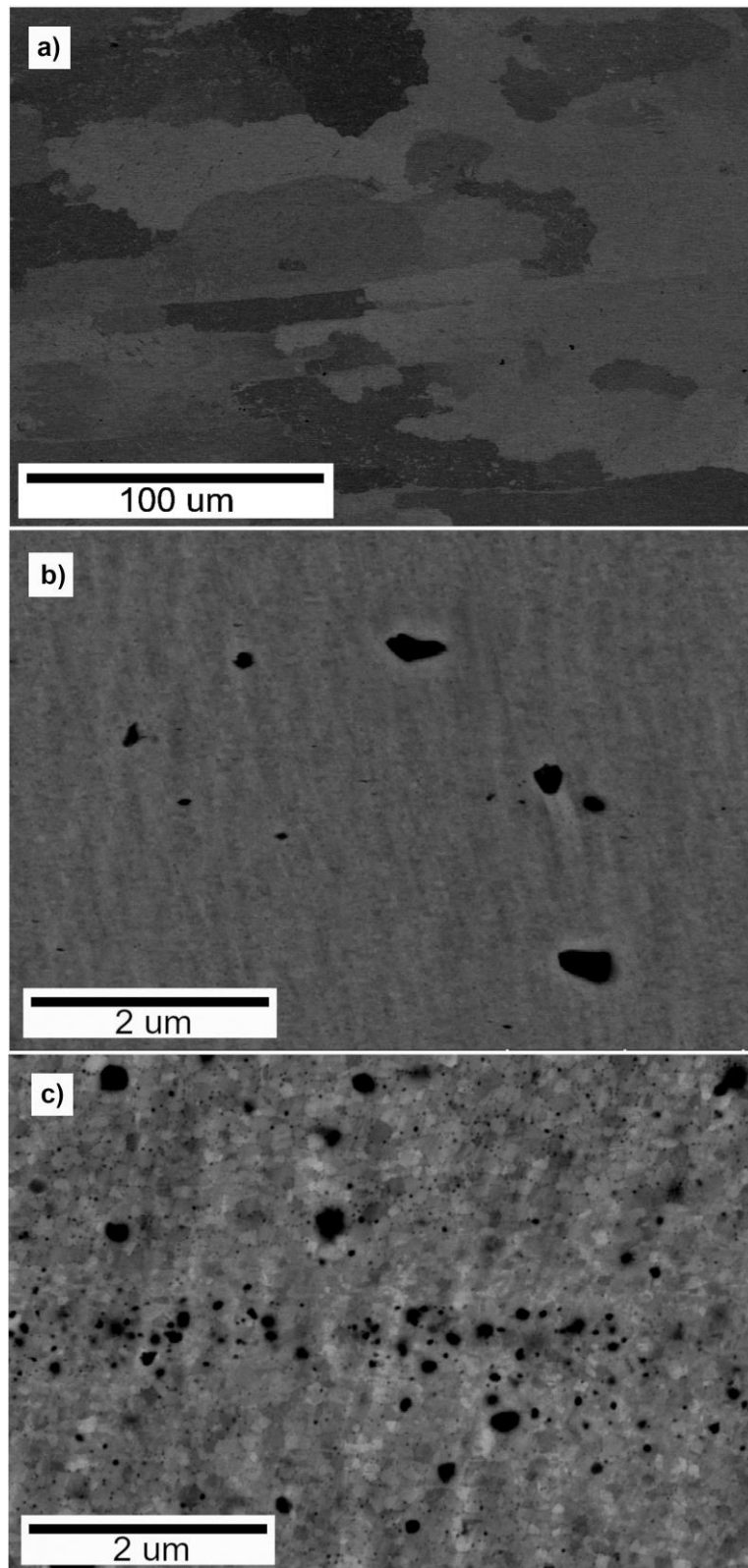*Figure 9 Hardness of the Cu-GO HPT nanocomposite and Cu HPT in function of annealing temperature*

Figure 10 SEM BSE image: a) Cu HPT after annealing at 300 ⁰C; b) Cu 1% GO HPT after annealing at 400 ⁰C; c) Cu 1% GO HPT after annealing at 500 ⁰C
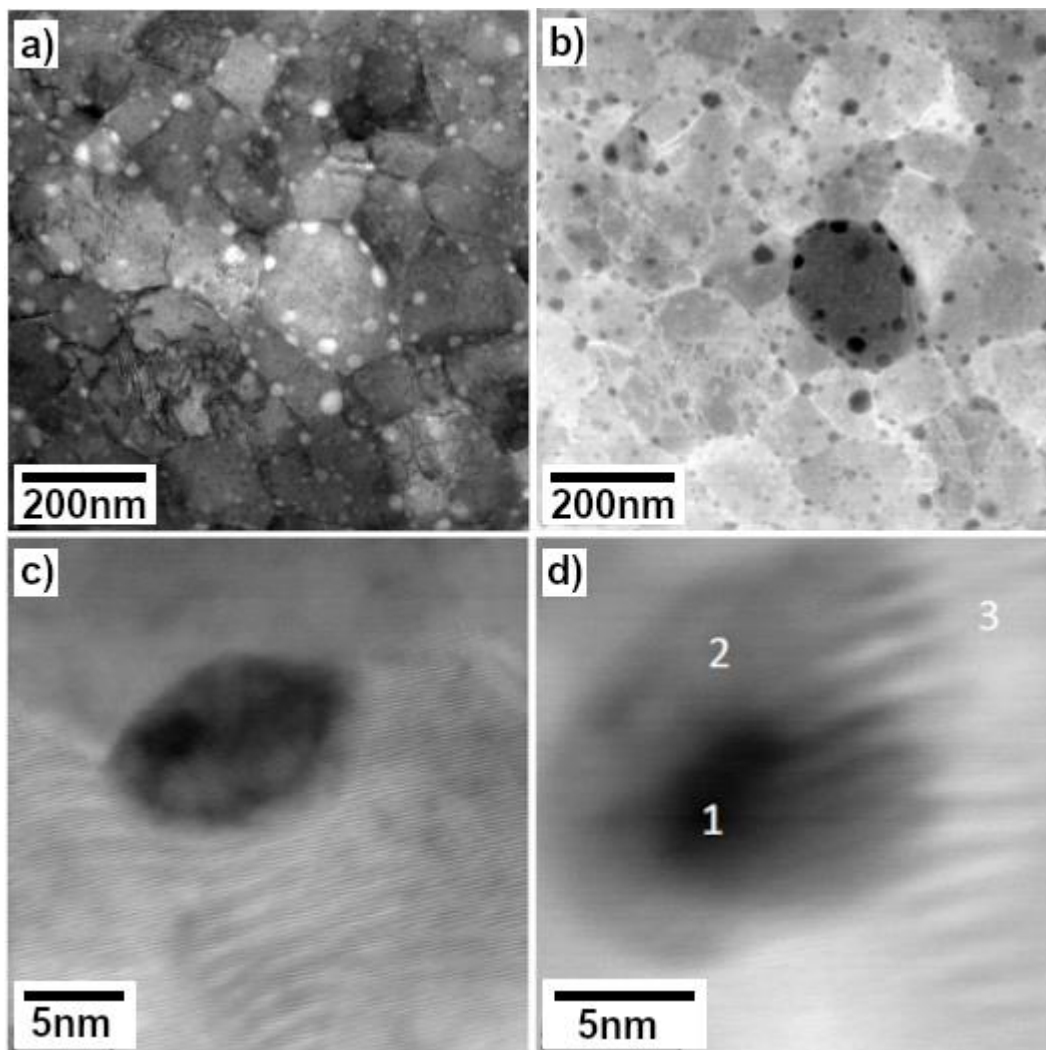
Figure 11 STEM image Cu-GO HPT after annealing at 500 °C with visible core shell structures trapped in Cu matrix: a) BF and b) HAADF, c) and d) STEM image of EDS measure points – core shell structure with carbon core, oxygen shell, trapped in Cu matrix